Numerical Studies of Ejecta Characteristics behind Thin Plates

M. Rosenblatt,* K. N. Kreyenhagen, and W. D. Romine
Shock Hydrodynamics Inc., Sherman Oaks, Calif.

A study of hypervelocity impact of spheres upon thin targets is described. The study was based upon numerical solutions utilizing the STEEP code. (STEEP is a two-dimensional Eulerian technique, based upon a hydrodynamic-elastic-plastic model.) The cases considered are Al, Cu, and Cd spheres impacting at 0.75 and 1.5 cm/μsec (24,600 and 49,200 fps) upon like-material target plates, with the plate thickness being $\frac{1}{4}$ of the projectile diameter. Results can be scaled to any impact case having the same ratio. From the numerical solutions, spatial plots showing the time-resolved response of the projectile and target are shown in the form of velocity, and principal stress fields. The primary objective of the solutions was to determine the characteristics of the debris clouds behind the targets. Curves are presented showing debris mass, axial momentum, and kinetic energy per unit solid angle intercepted on witness plates behind the targets. Information regarding the residual states of the debris materials is also given.

1. Introduction

HYPERVELOCITY impacts produce extreme pressures in the projectile and target materials. When the target is thin relative to the projectile dimensions, these propagate through to the rear surface, thereby accelerating the target material. Subsequent pressure rarefactions shatter the projectile and target materials, and a debris cloud is ejected at high velocity behind the target.

The effectiveness of thin metal plates in breaking up and dispersing compact hypervelocity projectiles into a cloud of tiny debris particles is the basis of "bumper" concepts for protecting structures against such impacts. With a properly selected bumper, the cumulative effect of the impacts of the debris particles on the protected structure will be less damaging than the effect of the original projectile. However, the debris itself will cause some damage to the protected structure, and means for absorbing the debris energy and for disbursing its momentum are sought. For the design of such absorbers, knowledge regarding the debris characteristics is needed. Experimental observations can be used to assess some debris characteristics, but such measurements are often difficult, and do not yield as complete a description as may be desired. Numerical techniques offer an alternative source of data, and can further be used to identify important mechanisms which operate in the formation and dispersion of the debris. In addition, numerical techniques can be applied to obtain data in experimentally inaccessible regions, e.g., extremely high impact velocities.

Two-dimensional numerical techniques have been developed and applied to a range of hypervelocity impacts into semi-infinite and relatively thick targets,[1–3] as well as into targets where the thickness is just sufficient to defeat the projectile.[4] Using the STEEP code, detailed solutions have now been obtained to study the debris characteristics in the seven thin plate impact cases in Table 1. The hydrodynamic-elastic-plastic model used in this code is described in Read.[5]

The numerical solutions of the seven cases treated permit a limited analysis of material property effects, impact velocity effects, and elastic-plastic strength effects. For these solutions, the projectile diameters were $\frac{1}{8}$ in. and the plate thicknesses were $\frac{1}{32}$ in. However, the results can be scaled to other impacts having the ratio of target thickness to sphere diameter, $T/D = \frac{1}{4}$.

Presented as Paper 69-356 at the AIAA Hypervelocity Impact Conference, Cincinnati, Ohio, April 30–May 2, 1969; submitted May 28, 1969; revision received December 29, 1969. This work was sponsored by the Air Force Materials Laboratory, Air Force Systems Command.

* Member, Senior Scientific Staff. Member AIAA.

2. Material Constitutive Relations

The elastic-plastic constitutive relations for aluminum, copper, and cadmium are specified by hydrodynamic equations of state, shear modulii, yield strengths, and dynamic tensile strengths. The hydrodynamic equations of state are given in terms of density and specific internal energy, i.e., $P = P(\rho,e)$. The shear modulii G, yield strength Y, and the dynamic tensile strengths $P_{\min}$ are assumed to be constant, with values as listed in Table 2.

A tabular equation of state was used for aluminum.[6] Entries in this tabulation were generated by consideration of porous Hugoniot data, the critical point, boiling point, and shear modulus, as well as the Thomas-Fermi theory and ideal gas behavior.

Most equations of state for copper and cadmium are valid only near the Hugoniot. For example, the Mie-Gruneisen equation of state permits a fair representation of states lying relatively close to the Hugoniot and would thus be adequate for calculations of an adiabat emanating from moderate shock pressure states (i.e., less than about 1 Mbar). However, in the impact cases in Table 1, impact pressures greater than 1 Mb occur. Thus equations of state valid off the Hugoniot are necessary. For cadmium, and also to a lesser extent for copper, an equation of state which degenerates to an ideal gas equation is appropriate. Tillotson[7] proposes a two part equation of state which has the required form. A transition curve separates the solid portion of the equation of state from the liquid-vapor portion. At small pressures and large volumes the ideal gas behavior is approximated by $P = (\gamma - 1)\rho e$. One objection to this form is that since the zero point for specific internal energy is taken at $P = 0$ and $\rho = \rho_0$ for the solid material, the ideal gas behavior should be given by $P = (\gamma - \rho 1)(e - e_s)$, where e_s is the sublimation energy. Another objection is that the formulation given by Tillotson allows for discontinuities in pressure along a portion of the transition curve. A modified Tillotson equation of state which avoids these difficulties was therefore developed. The transition line is chosen such that $\mu e = \mu_v e_v$, where $\mu = \rho/\rho_0 - 1$ and the subscript v refers to conditions at incipient vaporization. This line goes through the incipient vaporiza-

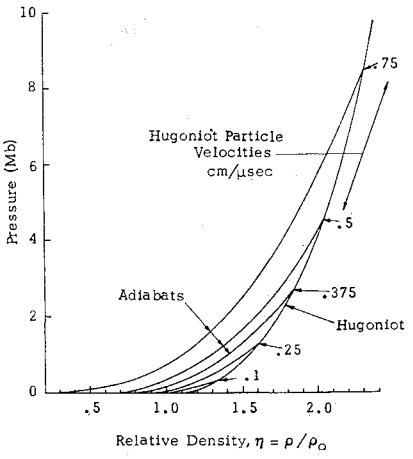

Fig. 1 Hugoniot and selected adiabats for cadmium.

tion point at $P = 0$ and then asymptotically to $\mu = 0$ in $P-\mu$ space. The complete formulation for the copper and cadmium equations of state,[6] reduces to the ideal gas equation, and the pressure and sound speed are continuous everywhere. Representative adiabats for cadmium appear in Fig. 1.

3. Qualitative Features of Thin Plate Impacts

The general characteristics of thin plate impacts will be illustrated using the numerical solution of case *A*, the Al/Al impact at 0.75 cm/μsec.

Velocity and Pressure Fields

Upon impact, a shock is established which travels from the interface into the target and also back into the projectile. Initially, this shock has a magnitude of 1.06 Mbar. Figure 2 is the velocity field at $t = 0.067$ μsec. The base of a velocity vector is located in each computational cell. The magnitude and direction of a vector refer to the average velocity of the mass in its cell. In all spatial plots in this paper, the horizontal scale is the axis of symmetry, and the vertical scale is radius. Square computational cells were used throughout, with a grid spacing of $\frac{1}{160}$ in. In all the spatial plots which will be shown, horizontal and vertical grid lines are shown at spacings of $\frac{1}{32}$ in. The small circles connected by straight lines represent free surfaces. Three annular target sections are delineated by small *x*'s. The distortion these regions undergo will be commented on in a later spatial plot.

Figure 3 shows the velocity field at 0.16 μsec. At this time, rarefaction waves from the target rear surface are propagating back into the shocked material. These relief waves reduce the stresses and further accelerate the target material. Thus a large bulge is produced in the target, but the bulging material is now subjected to only small stresses. It is also seen that the shock and rarefaction systems are beginning to cause some radial dispersion of the target and projectile mass.

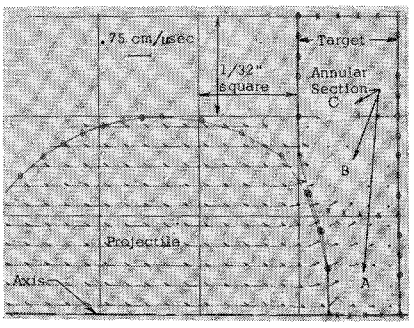

Fig. 2 Velocity field at 0.067 μsec (case A: Al vs Al at 0.75 cm/μsec).

Table 1 Impact cases

Case	Projectile and target material	Impact velocity, cm/μsec	Impact Hugoniot pressure, Mbar
A-Hydro	Al	0.75	1.06
A	Al	0.75	1.06
B	Al	1.5	3.12
C	Cu	0.75	3.24
D	Cu	1.5	10.45
E	Cd	0.75	2.69
F	Cd	1.5	8.61

Figure 4 shows the principal stress field at 0.315 μsec. In stress plots, the two principal directions in the *r-z* plane are plotted, being always orthagonal. The third principal direction in axially symmetric cases is in the azimuthal direction, and it is plotted along a diagonal. Vectors pointing to the right denote compression; to the left, tension. It is seen that the large stresses are concentrated in two separate regions. One is the pulse traveling radially (outward) in the target. It will subsequently attenuate due to geometrical divergence and due to relaxation from the target surfaces. The other highly stressed region is in the rear of the projectile. The pressures here are approximately 15–20% of the initial impact pressures. These will subsequently be further relieved by the rarefaction from the back surface of the projectile, as well as by the continuing rarefaction from the rear surface of the target.

The final computed velocity field, at 0.8 μsec, is shown in Fig. 5. An annular "necked" region has formed between the debris cloud and the target material. The projectile-target is shown, as well as the boundaries of the annular target regions originally delineated in Fig. 2. The shapes of these regions indicate the distortion which the annular sections of the target have suffered.

By 0.8 μsec, stresses, or pressures, in the debris cloud have dropped to a low level (<1 kbar), so that no significant further accelerations will develop in the debris cloud. Thus the elements of the debris mass will continue to travel approximately as indicated by the magnitudes and directions of the local velocity vectors in Fig. 5. From the velocity field, it is seen that the necking material and also the target mass near the neck will become part of the debris cloud. Some of the disturbed target mass, however, will remain attached to the target. A portion of this disturbed mass will be permanently deformed and the rest will elastically recover.

Apparent Radiating Point

The debris cloud in Fig. 5 shows that greater divergence occurs with increasing radii (i.e., the velocity vectors make larger angles with the axis at larger radii). The velocity vectors also tend to become larger in magnitude at greater distances behind the target. These velocity gradients will cause the debris cloud to expand both radially and axially at later times. For example, consider the mass near the axis of symmetry, where the velocity is parallel to the axis. The speed of this mass is a minimum at the trailing edge of the debris (the projectile rear surface), and increases along the axis to approximately the impact velocity at the leading edge of the cloud (the target rear surface). All the debris mass has a forward velocity, and thus an expanding hollow cavity forms between the original target and the debris cloud.

Table 2 Material properties

Material	*G*, Mb	*Y*, Mb	P_{min}, Mbar
Al	0.259	0.00276	−0.03
Cu	0.451	0.00345	−0.06
Cd	0.241	0.00071	−0.001

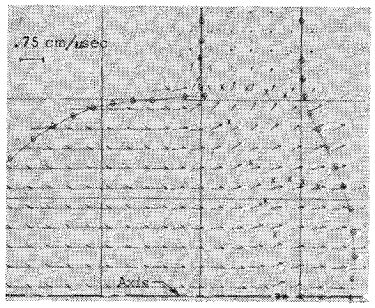

Fig. 3 Velocity field at 0.16 μsec (case A).

The velocity vectors in Fig. 5 fan out in a manner which suggests that they emanate from a single radiating point, as in the sketch in Fig. 6. To establish whether such a single radiating point may reasonably be assumed, the points where the velocity vectors from each computational cell intercept the axis were established. Averages of the intersections (z-values) were then obtained. For all impact cases, this average fell approximately one projectile diameter in front of the target (that is, at a point on the axis corresponding to the projectile rear surface at the moment of impact) with standard deviations of about one diameter. Thus, while all the debris mass does not diverge from exactly the same point the variation is small compared to witness plate spacings of probable interest.

Hole Size

The primary objective of the impact calculations was to determine the characteristics of debris behind the thin-plate targets. Of particular interest were those characteristics which could lead to significant damage to protected structures behind the thin plate. The hole sizes in the targets were therefore of interest only insofar as the properties of the mass of material removed in making the hole would contribute to the over-all characteristics of the debris cloud.

In Fig. 5, it is observed that the main body of the debris is rapidly disengaging from the target in the necking region, and that the axial component of velocity sharply declines in the target material at radii beyond the neck. Even though some of this target material will subsequently break off and become part of the debris, it will be traveling at low velocities and will contribute little to the damage potential of the debris cloud in terms of kinetic energy or momentum. Thus the important debris characteristics are not significantly altered by target mass coming from near the periphery of the hole which is formed, and are hence insensitive to the exact size of the hole.

Debris Mass, Momentum, and Energy

From the computed data at the last integration cycle, an extrapolation routine can be used to predict the mass, momentum, and energy which will be incident upon witness plates placed at any specified range in the path of the debris cloud. However, since it is shown herein that the debris nominally emanantes from an apparent radiating point, it is

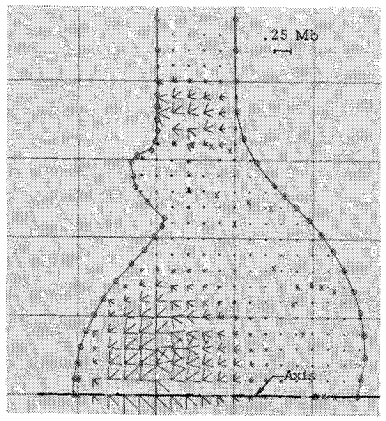

Fig. 4 Principal stresses at 0.32 μsec (case A).

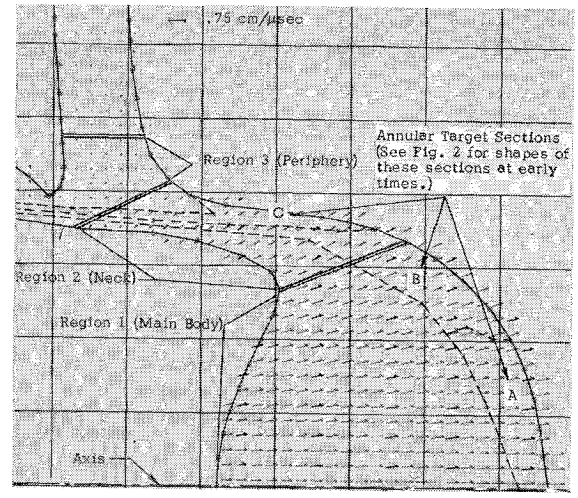

Fig. 5 Velocity field at 0.8 μsec (case A).

convenient to express debris data in terms of quantities per unit solid angle (i.e., solid angle densities). Given data in solid angle form, the debris characteristics which will impact on a witness plate (or protected structure) at any spacing can be easily determined.

Figure 7 shows debris mass, axial momentum, and kinetic energy solid angle densities vs solid angle for the Al-Al impact at 0.75 cm/μsec. The debris quantities have been normalized by dividing by the corresponding properties for the impacting projectile.

It is seen that the largest concentration of debris mass, momentum, and energy occurs for small solid angles, i.e., near the axis. (The close-in-irregularities in the curves at about $\Omega = 0.05$ are due to mass fluctuations in the computational cells near the axis, and are not physically realistic.) Further from the axis, the height of the mass curve compared to the corresponding momentum and energy curves indicates that the mass which is remote from the axis has relatively low velocity.

Sharp discontinuities in the slopes of all the curves are seen at solid angles of approximately 0.35 and 0.9 steradians, (corresponding to included half-angles of 19.5° and 31°, respectively). These slope discontinuities have been labeled Ω_a and Ω_b. There should be corresponding discontinuities in the damage caused to witness plates at radii equivalent to Ω_a and Ω_b.

The positions of the slope discontinuities can be related to the origin of the debris involved. In the velocity field plot in Fig. 5, three regions are delineated. Region 1, the main body of the debris cloud, is primarily composed of projectile material and target material coming from an area of the target with radius less than the original projectile radius. Region 2 is composed of most of the expanding annular neck. Region 3, the periphery of the debris, contains target mass from the base of the neck out to the final target hole radius. These are not precisely defined regions, of course, and the lines separating the regions in Fig. 5 are intended only to indicate the nominal location of the boundaries. The boundary between regions

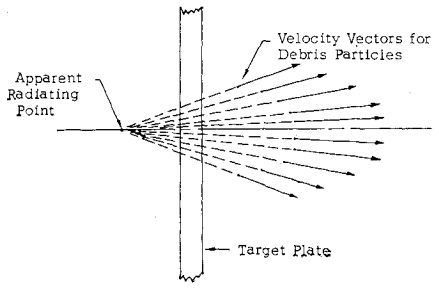

Fig. 6 Concept of apparent radiating point.

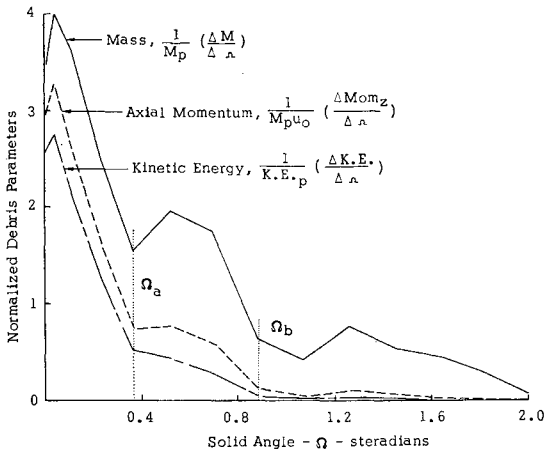

Fig. 7 Solid angle densities of debris characteristics vs solid angle (case A).

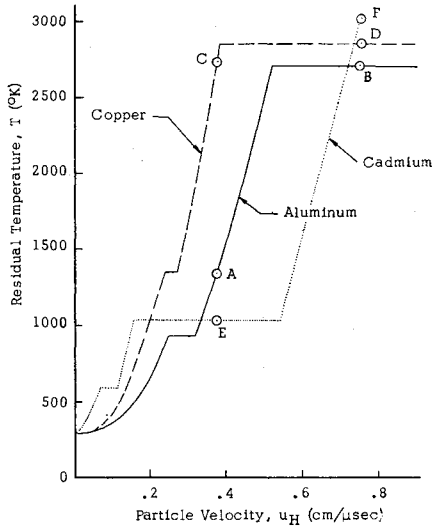

Fig. 8 Residual temperature vs Hugoniot particle velocity.

1 and 2 corresponds approximately with the solid angle value at which the first discontinuity appears in Fig. 7 (at $\Omega_a = 0.35$). Similarly, the boundary between regions 2 and 3 roughly corresponds with the solid angle value of the second discontinuity in Fig. 7 (at $\Omega_b = 0.9$). This suggests that the debris characteristics between 0 and Ω_a are primarily contributed by Region 1 (the main body), while Region 2 (the neck) is primarily responsible for the debris characteristics between Ω_a and Ω_b. Region 3 (the peripheral debris) contributes the relatively small quantities beyond Ω_b. In reality, of course, not all particles radiate from exactly the same apparent point, and there is some overlap in the contributions of the regions to the debris characteristics.

4. Total Mass, Axial Momentum, and Energy in Debris Clouds

The gross debris characteristics can be expressed in terms of the total mass, axial momentum, kinetic energy, and internal energy. In hypervelocity impacts against thin targets, most of the axial momentum and energy after perforation are found in the debris cloud. However, there is some axial momentum and energy associated with the material which splashed off the front surface of the target. The sum of the mass in the debris cloud and in the splash after impact equals the initial projectile mass plus the mass of target material removed (i.e., the hole). The sum of the momentum in the debris, splash, and in the target must have an axial component equal to the initial projectile momentum. And, the sum of the kinetic and internal energies in the debris, splash, and target must equal the kinetic energy of the projectile.

Table 3 contains the initial projectile masses, momenta, and kinetic energies for the seven impact cases which have been analyzed, and shows the final debris cloud masses, momenta, and energies, expressed in normalized form by dividing by the corresponding initial projectile characteristics. (In Table 3 and in the text which follows, the subscript P refers to the initial projectile quantities.) Table 3 also contains the debris mass, M, as a fraction of the total free mass. (Free mass refers to all material not attached to the target, and is thus the total of the projectile mass and the mass of the hole removed from the target, i.e., $M_{free} = M_P + M_{hole}$.)

5. Final States of the Debris Clouds

The specific internal energy at a point in the debris cloud will remain constant with time once the zero pressure equilibrium state is reached. This value will be referred to as the residual specific internal energy. The initial and residual values of specific internal energy depend, in general, on the peak pressure experienced by a mass element. The higher the peak pressure the higher the values of initial and residual specific internal energies. In our cases, the peak pressures result from the impact shock waves. Near the impact point, where the initial shock particle velocities lie on the Hugoniot and have a value of $u_H = u_0/2$ for similar material impacts, the initial specific internal energy is given by $e_H = u_H^2/2 = u_0^2/8$. The subscript H refers to conditions on the shock Hugoniot and u_0 is the impact velocity. At locations other than near the impact point, the projectile and target materials will experience less intense pressures and will thus have lower initial and residual specific internal energies. Thus, since the rear of the projectile experiences lower pressures than the front, the residual specific internal energy near the rear of the projectile will be lower than the values near the impact point. The magnitude of the residual specific internal energy can be

Table 3 Debris characteristics

Impact case	Projectile Mass M_p, g	Axial mom., g-cm/μsec	Kinetic energy, $(K.E.)_p$, 10^{12} ergs	Normalized debris parameters: Debris mass, M/M_p	Debris mass / free mass, M/M_{Free}	Axial mom., $Mom_z/M_p u_p$	Kinetic energy, K.E./$(K.E.)_p$	Internal energy, I.E./$(K.E.)_p$	Total energy, K.E. + I.E./$(K.E.)_p$
A-Hydro	0.045	0.034	0.013	3.8	0.95	1.23	0.82	0.16	0.98
A	0.045	0.034	0.013	2.9	0.92	1.15	0.81	0.16	0.97
B	0.045	0.068	0.051	2.7	0.84	1.08	0.84	0.12	0.96
C	0.150	0.113	0.042	3.6	0.92	1.19	0.81	0.15	0.96
D	0.150	0.225	0.169	2.9	0.74	1.09	0.84	0.11	0.95
E	0.145	0.109	0.041	3.1	0.78	1.10	0.85	0.10	0.95
F	0.145	0.217	0.163	2.6	0.66	1.05	0.89	0.08	0.97

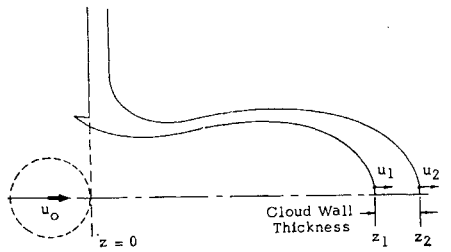

Fig. 9 Quantities defining axial expansions.

directly related to the residual temperature and to the residual state—solid, liquid, or vapor.

In this study, the final debris states at zero pressure were determined using the material equations of state, the first law of thermodynamics, and the thermodynamic properties of the materials. The high pressures and short time scales involved in impacts permit the assumptions that heat transfer in the debris cloud is negligible, and that distortional energy contributions to internal energy are negligible. The complete set of adiabatic equations, including the particle velocity equations for a rarefaction wave are

$$de = Pd\rho/\rho^2 \quad (1)$$

$$du = \pm cd\rho/\rho \quad (2)$$

$$c^2 = (\partial P/\partial\rho)_{\text{entropy}} = (\partial P/\partial\rho)_e + (P/\rho^2)(\partial P/\partial e)_\rho \quad (3)$$

The adiabatic assumption permits an analytical evaluation of the residual energy at $P = 1$ atm for any initial pressure, density, and specific internal energy state. However, for determining the highest state of residual energy, only initial states lying on the Hugoniot need to be considered.

In Fig. 1, series of adiabats centered on the Hugoniot which were calculated for cadmium are shown. Similar information was generated for aluminum and copper. Equation (1) was evaluated down these release adiabats to yield the specific residual energies at the final pressures (i.e., $P \cong 0$). These residual energies were then converted to residual temperatures using the tabulated values given in Stull and Sinke.[8]

Figure 8 shows the residual temperatures which result in the three materials as a function of the Hugoniot particle velocity. (For similar material impacts, this is half the impact velocity.) The states produced by the impact cases in Table 1 are shown in Fig. 8 by the circles and corresponding letters. Note that as the shock strength and particle velocities increase, the residual temperatures monotonically increase until the melting or vaporization temperatures are reached. At these temperatures, plateaus occur, i.e., an increase in shock strength does not increase the residual temperature. Additional internal energy from the increased shock strength is required to accomplish the solid-liquid or liquid-vapor phase transition. The lower end of each plateau corresponds to the incipient phase change condition, while the higher end represents the completed phase change. At intermediate points, such as point E on the Cd curve in Fig. 8, part of the material is in each state.

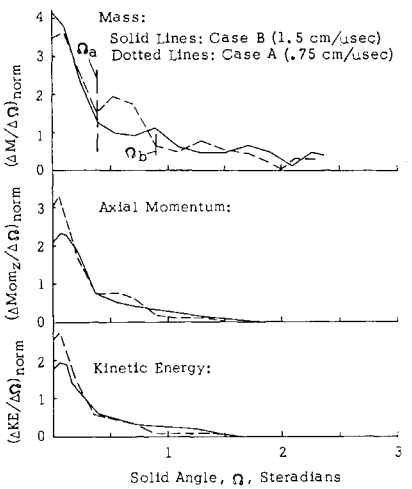

Fig. 10 Normalized debris, mass, axial momentum, and kinetic energy solid angle densities vs solid angle for aluminum impact cases.

For the impact cases discussed herein, Table 4 gives the pressures, particle velocities, specific residual energies, residual temperatures, and residual states attained by target and projectile materials close to the impact point, and also for projectile materials near the rear surface of the projectile. The conditions for material near the impact point represent the maximum conditions which are achieved. Elsewhere, rarefactions from free surfaces reduce the peak shock pressures. Thus the debris cloud will be composed of materials having residual conditions ranging up to those listed in Table 4 for material near the impact.

A relatively constant ratio of about 0.2 was observed between the residual specific internal energy (e_r) and the initial Hugoniot energy (e_H) for Al, Cu, and Cd for all shock states

Table 4 Hugoniot pressures and residual energies, temperatures, and states for material near impact point and material near rear of projectile

	Material near impact point				Material near rear of projectile			
Impact case	Hugoniot pressure P_H, Mbar	Residual internal energy, $10^{12}\frac{\text{ergs}}{\text{g}}$	Residual temp. T_r, °K	Residual state	Hugoniot pressure P_H, Mbar	Residual internal energy $10^{12}\frac{\text{ergs}}{\text{g}}$	Residual temp. T_r, °K	Residual state
A	1.06	0.015	1350	liquid	0.18	0.00058	350	solid
B	3.12	0.048	2720	liquid/ vapor	0.70	0.0082	930	solid/ liquid
C	3.24	0.014	2740	liquid, incipient vapor	0.62	0.0012	610	solid
D	10.45	0.051	2855	liquid/ vapor	1.9	0.0077	1560	liquid
E	2.69	0.010	1038	liquid/ vapor	0.59	0.0019	800	liquid
F	8.61	0.014	3030	vapor	2.3	0.0089	1040	liquid/ vapor

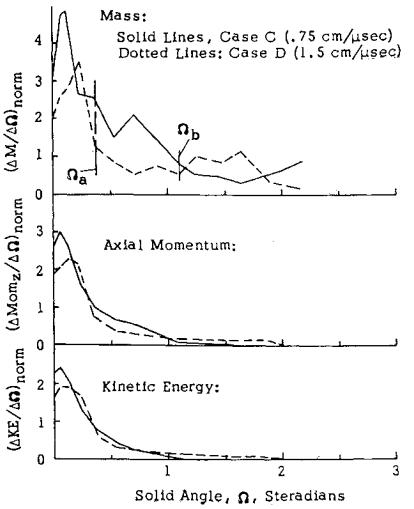

Fig. 11 Normalized debris, mass, axial momentum, and kinetic energy solid angle densities vs solid angle for copper impact cases.

having residual energies up to the incipient vaporization level.[6]

The lower boundary of residual conditions for debris material coming from the projectile is established by the shock strength reaching the rear (trailing) surfaces of the projectile. These peak shock values and the corresponding residual conditions are also given in Table 4.

Even lower residual conditions will occur in those parts of the debris cloud consisting of target material originating near the periphery of the hole, since this material will experience only relatively weak stress waves and will remain in the solid state. Indeed, this will be the case for any impact against a solid target. Regardless of the impact velocity and the peak pressures near the impact point, some material in the debris cloud (i.e., that material originating near the hole periphery) will always be solid.

6. Expansion of the Debris Cloud

In Figure 9, the axial parameters which are used to define the cloud expansion are defined. z represents displacement from the impacted surface and u is particle velocity. At late times, $z \approx ut$.

In comparing debris clouds from the impact solutions, three ratios will be used. The ratio $z_1/z_2 \approx u_1/u_2$ represents the

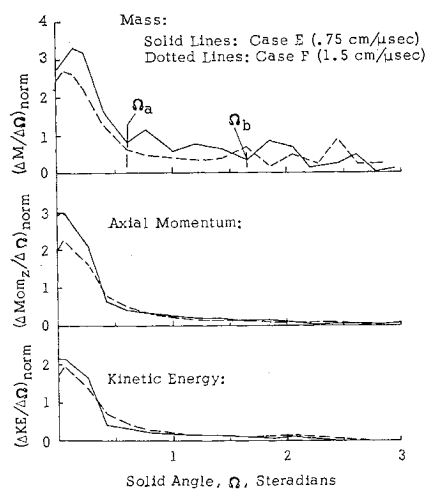

Fig. 12 Normalized debris, mass, axial momentum, and kinetic energy solid angle densities vs solid angle for cadmium impact cases.

size of the hollow cavity relative to the over-all cloud size, or the degree of "hollowness" of the cloud. The ratio of cloud wall thickness $(z_2 - z_1)$ to maximum cloud displacement, or $(z_2 - z_1)/z_2 \approx (u_2 - u_1)/u_2$, characterized the axial spreading of the cloud wall material. (For convenience, the forms of these ratios will be used. At late times, these ratios are essentially time-independent.) A third ratio, u_2/u_0, indicates the maximum velocity of the cloud, normalized to the impact velocity.

Table 5 summarizes the spread ratio, hollowness ratio, and normalized maximum velocity for the debris clouds formed by the seven impact cases.

Note that the normalized maximum velocities, u_2/u_0 are all near a value of 1, indicating that the leading edge of the cloud travels at approximately the impact velocity. The particles which make up this leading edge originate on the rear free surface of the target near the axis. The shock introduced in the target by impact produces particle velocities equal to half the impact velocity. Rarefaction waves which relieve the high pressures also produce particle accelerations. Sources of such pressure relief are the free surfaces of the target and the projectile, such that the rarefaction wave system is two-dimensional in nature. However, for target material near the axis in relatively thin targets (such as were considered here), the predominate source of pressure relief will be the rear free surface of the target. The resulting rarefaction wave will therefore be essentially one-dimensional (parallel to that surface). This wave is then responsible for further acceleration of the moving material near the rear surface to a velocity approximately equal to the impact velocity.

The debris spread can be correlated with the residual conditions given in Fig. 8 in that as the residual state more closely approaches the vapor condition, the normalized maximum cloud velocities and the spreading of the cloud walls increase, while the hollowness decreases. Thus clouds containing a high percentage of vapor are faster and more diffuse.

Although the data in Table 5 indicate that the debris clouds will be hollow, the spreading of the leading surface of the cloud is greater than is observed experimentally.[9] Thus the numerical solution indicates a relatively diffuse hollow cloud wall, while experiments show a sharply defined, relatively narrow cloud wall having more the appearance of an expanding bubble. Since the spreading of the wall is due to differences in velocity between the leading and trailing edges, the numerical solution has apparently predicted too low a velocity for the trailing edge. Such could be the case if the peak pressure calculated to reach the back surface of the projectile is too high, or if the dynamic tensile strength (P_{min}) is too low. Either of these possibilities would be related to the material model and properties used. Inclusion of strain rate and dynamic tensile effects, for example, might be expected to reduce the velocity gradient through the cloud wall.

7. Mass, Axial Momentum, and Kinetic Energy Solid Angle Densities

The solid angle densities of forward debris mass $(\Delta M/\Delta\Omega)$, axial momentum $(\Delta Mom_z/\Delta\Omega)$ and kinetic energy $(\Delta KE/\Delta\Omega)$

Table 5 Debris spread and expansion

Impact case (see Table 1)	Spread ratio, $(u_2 - u_1)/u_2$	Hollowness ratio, u_1/u_2	Normalized max. vel., u_2/u_0
A-Hydro	0.22	0.78	0.94
A	0.23	0.77	0.92
B	0.37	0.63	1.00
C	0.28	0.72	0.94
D	0.41	0.59	1.05
E	0.41	0.59	1.07
F	0.50	0.50	1.17

are plotted vs solid angle in Figs 10, 11 and 12 for six impact cases. In all cases, the debris quantities have been normalized by dividing by the corresponding initial projectile properties.

Impact Velocity Effects

The curves in these figures show similar slope discontinuities, identified as Ω_a, in all the parameters at both velocities. The value of Ω_a is insensitive to the impact velocity. In the curves for the lower velocity cases, a less distinct discontinuity appears at Ω_b, but no corresponding discontinuity is perceptible in the higher velocity cases. (The significance of Ω_a and Ω_b is discussed under heading 3 above.) The greatest concentration of debris mass, momentum, and energy always occurs in solid angles less than Ω_a. Increased impact velocity, however, leads to lower normalized values of these parameters. This is apparently due to increased radial expansion of the cloud from the greater internal energies in higher velocity impacts. (The above comments refer only to the normalized parameters. The absolute values of debris momentum and energy are of course higher for the 1.5 cm/μsec impacts than for the 0.75 cm/μsec cases.)

Material Effects

Although certain differences are apparent between the debris characteristic curves for the three materials, the degree of similarity is noteworthy. The discontinuities at Ω_a are seen to occur at essentially the same solid angle value for all three materials (i.e., $\Omega_a \approx 0.4$, corresponding to an angle of about 20°).

The predominately vaporous state of the cadmium debris at both velocities cause this material to have the lowest concentration of normalized mass, axial momentum, and kinetic energy near the axis. However, note that in the high impact velocity cases, the axial momentum and kinetic energy curves are nearly identical for the three materials treated. In the high-velocity impacts, all the materials produce debris clouds which are at least partially in the vapor state.

8. Influence of Elastic-Plastic Effects

Impact Cases A and A-hydro used identical initial conditions, except that in A-hydro a purely hydrodynamic model was used (i.e., G and Y in Table 2 were set to zero). A comparison of these cases shows the effect of elastic-plastic properties upon the debris cloud.

The neglect of elastic-plastic effects results in a larger hole in case A-hydro than is found in case A, thereby producing a correspondingly larger debris mass (see Table 3). There is also greater axial momentum in the debris cloud from the purely hydrodynamic impact. This is due partly to the increased mass, but, in addition, the elastic-plastic properties in case A permit more rapid propagation of relief waves into the high pressure region, thereby reducing particle velocities to a lower level than in case A-hydro.

Omission of material strength has only a small effect on cloud expansion characteristics, as is seen in Table 5.

Figure 13 compares the normalized debris mass, axial momentum, and kinetic energy solid angle densities vs solid angle for case A and case A-Hydro.

In the hydrodynamic solution, the larger hole size leads to the larger total debris mass which is evident in Fig. 13 (i.e., the total area under the mass per unit solid angle curve is greater for Case A-Hydro). The differences between the momentum and energy curves for the two solutions, however, are quite small, indicating that the velocity of the incremental mass near the periphery of the hole for case A-Hydro is quite small.

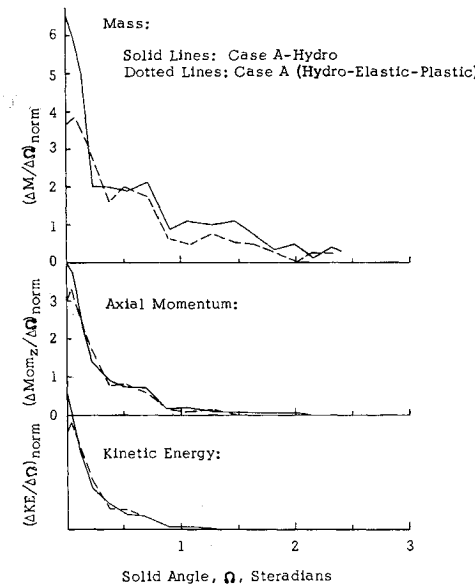

Fig. 13 Normalized debris, mass, axial momentum, and kinetic energy solid angle densities vs solid angle for the purely hydrodynamic and the hydrodynamic-elastic-plastic solutions of the 0.75 cm/μsec aluminum impact.

The mass curves in Fig. 13 show a significantly smaller mass concentration near the axis for the impact where elastic-plastic effects were considered, again due to the fact that rarefaction waves propagate more rapidly with the elastic-plastic model.

From these comparisons, it is evident that elastic-plastic material properties exercise some effect upon characteristics of the debris cloud, even for the relatively thin target plates considered. Where thicker targets are involved, the influence of material strength will become more important.

References

[1] Bjork, R. L., "Effects of a Meteoroid Impact on Steel and Aluminum in Space," *Proceedings of the Tenth International Astronautical Congress*, Springer-Verlag, London, 1959, p. 505.

[2] Bjork, R. L., "Review of Physical Processes in Hypervelocity Impact and Penetration," *Proceedings of the 6th Symposium on Hypervelocity Impact*, Colorado School of Mines, Vol. II, Pt. I, 1963, pp. 1–58.

[3] Walsh, J. M. and Tillotson, J. H., "Hydrodynamics of Hypervelocity Impact," *Proceedings of the 6th Symposium on Hypervelocity Impact*, Colorado School of Mines, Vol. II, Pt. I, 1963, pp. 59–104.

[4] Kreyenhagen, K. N., Wagner, M. H., and Bjork, R. L., "Ballistic Limit Determination in Impacts on Multi-Material Laminated Targets," AIAA Paper 69-356, Cincinnati, Ohio, 1969.

[5] Read, H. E., "Hardening Technology Studies II, STRIDE, A Three-Dimensional Code," LMSC-D00017, 1967, Lockheed Missiles and Space Co., Sunnyvale, Calif.

[6] Rosenblatt, M., Kreyenhagen, K. N., and Romine, W. D. "Analytical Study of Debris Clouds Formed by Hypervelocity Impact on Thin Plates," AFML-TR-68-266, Air Force Materials Lab., Wright-Patterson Air Force Base, Ohio, 1968.

[7] Tillotson, J. H., "Metallic Equations of State for Hypervelocity Impact," GA3216, 1962, San Diego, Calif., General Atomics.

[8] Stull, D. R. and Sinke, G. C., "Thermodynamic Properties of the Elements," 1956, Washington, D. C., American Chemical Society.

[9] Swift, H. F. et al., "Characterization of Debris Clouds Behind Impacted Meteoroid Bumper Plates," AIAA Paper 69-379, Cincinnati, Ohio, 1969.